Simulation of seismic triggering and failure time perturbations associated with the 30 October 2020 Samos earthquake (Mw 7.0)

Eyüp SOPACI[1,*] 🔲 , **Atilla Arda ÖZACAR[1,2]** 🔲

[1] Geodesy and Geographic Information Technology, Middle East Technical University, Ankara, Turkey
[2] Department of Geological Engineering, Faculty of Engineering, Middle East Technical University, Ankara, Turkey

Abstract: The 30 October 2020 Samos earthquake (Mw = 7.0) ruptured a north-dipping offshore normal fault north of the Samos Island with an extensional mechanism. Aftershocks mainly occurred at the western and eastern ends of the rupture plane in agreement with the Coulomb static stress changes. Mechanism of aftershocks located west of the rupture supported activation of the neighboring strike-slip fault almost instantly. In addition, a seismic cluster including events with Mw~4 has emerged two days later at the SE side of Samos Island. This off-plane cluster displays a clear example of delayed seismic triggering at nearby active faults. In this study, numerical simulations are conducted to mimic the instant and delayed seismic triggering observed after this event and evaluate resultant seismic cycle perturbations at adjacent faults and near İzmir, where amplified ground motions caused heavy damage. For this purpose, Coulomb static stress changes and seismic waveforms recorded by strong-motion stations are combined as static and dynamic triggers on a rate-and-state friction dependent quasi-dynamic spring slider model with shear-normal stress coupling. According to our results, earthquakes with Mw ≤ 3.5 can be triggered instantly, and Mw ≥ 4 events noticeably advance in failure time. However, instant triggering occurs only when static stress loading is very high, and the fault is close to fail, explaining the delayed triggering observed SE of Samos Island. Simulations also revealed that the shear-normal stress coupling increases static loading but does not affect the dynamically controlled failure time advances observed at the end of the seismic cycle. After the earthquake, some of the faults adjacent to the rupture are more likely to fail, especially the long strike-slip fault segment capable of generating large earthquakes at the western edge. On the other hand, the Samos earthquake induced no significant dynamic triggering on far away faults near İzmir.

Key words: Earthquake triggering, failure time advance, rate-and-state friction, quasi-dynamic

1. Introduction

The 30 October 2020 Samos earthquake (Mw 7.0) ruptured the North dipping normal fault located North of the Samos Island (Kiratzi et al., 2020). Previous time-dependent seismicity studies using probabilistic approaches suggested the region being a nest for a not-too-distant-future large earthquake (Karakaisis, 2000; Coban and Sayil, 2019). The ground shake felt in Turkey and Greece caused fatal casualties in the Metropolitan city İzmir and Samos Island. Nevertheless, the most mattering question afterward was if the Samos rupture brings the surrounding faults close to failure, increasing seismic risk. Previously, Coulomb static stress changes are commonly used to assess seismic triggering (King et al., 1994). Recently, the two-day apart Ridgecrest earthquakes (Mw 6.4 followed by Mw 7.1) on 4 and 5 July 2019 revive the efforts to understand large earthquakes' triggering (Nanjo 2020). In Turkey, such triggering of damaging earthquake was also proposed for the 17 August 1999 İzmit (Mw 7.4) and 12 November 1999 Düzce (Mw 7.2) earthquakes that ruptured neighboring segments of the North Anatolian Fault several months apart (Cakır et al., 2003).

The traditional belief for earthquake triggering is that permanent stress transfer increases stress level in the vicinity of a rupture and triggers faults in short distances. In contrast, dynamic effects reach far distances and trigger small earthquakes. This definition is not entirely false but rather

incomplete. Kilb et al. (2000) showed the first evidence to the best of our knowledge that the dynamic triggering causes asymmetry patterns in the seismicity rate. This asymmetry disappears when only static triggering is responsible for triggered seismicity. Today we know that not only static stress loadings advance (or delay) the clock of an earthquake in nearby faults, but transient signals alter the frictional state and lead to a further clock advance.

A useful approach to understanding the static and dynamic triggering is the rate-and-state friction (RSF) (Dieterich, 1979; Ruina, 1983). Many numerical simulations were conducted on single-degree-of-freedom (SDF) models (Gomberg et al., 1997, 1998; Belardinelli et al., 2003; van der Elst and Savage, 2015) and in a 2D continuum models (Perfettini et al., 2003a, 2003b; Yoshida, 2018). Besides, laboratory works contributed to understanding the physical mechanisms and dominance of static and dynamic effects individually (Beeler and Lockner 2003; Savage and Marone, 2007). We previously tested the miscellaneous views of friction on a pure vertical strike-slip fault triggered by static and dynamic signals (Sopaci and Özacar, 2020).

The Samos earthquake occurred in a complex region where both strike-slip and normal faults indicate an ongoing transtensional tectonic regime. The observed almost instant triggering of neighboring strike-slip fault in the west and two-day delayed triggering of a seismic cluster at the SE side of the

Samos Island provided much-needed observational data to analyze seismic triggering (Figure 1). In this study, we first computed the Coulomb static stress changes using a homogeneous slip model to reveal stress loading at nearby fault segments. Next, relocated aftershocks are analyzed both in space and time to establish the nature of seismic triggering at different aftershock clusters. Then, the seismic triggering cases observed after the Samos earthquake are simulated using RSF dependent SDF model with normal-shear stress coupling relation (Linker and Dieterich, 1992). Unlike previous studies, both static and dynamic effects are considered during numerical simulations by utilizing computed Coulomb static stress changes and recorded strong motion waveforms as triggering signals simultaneously, which provided a unique opportunity to evaluate their relative role in a given triggering scenario. The results shed light on the conditions favoring instant and delayed seismic triggering, which are crucial to realistically evaluate the seismic triggering potential of an earthquake at nearby and far away fault segments.
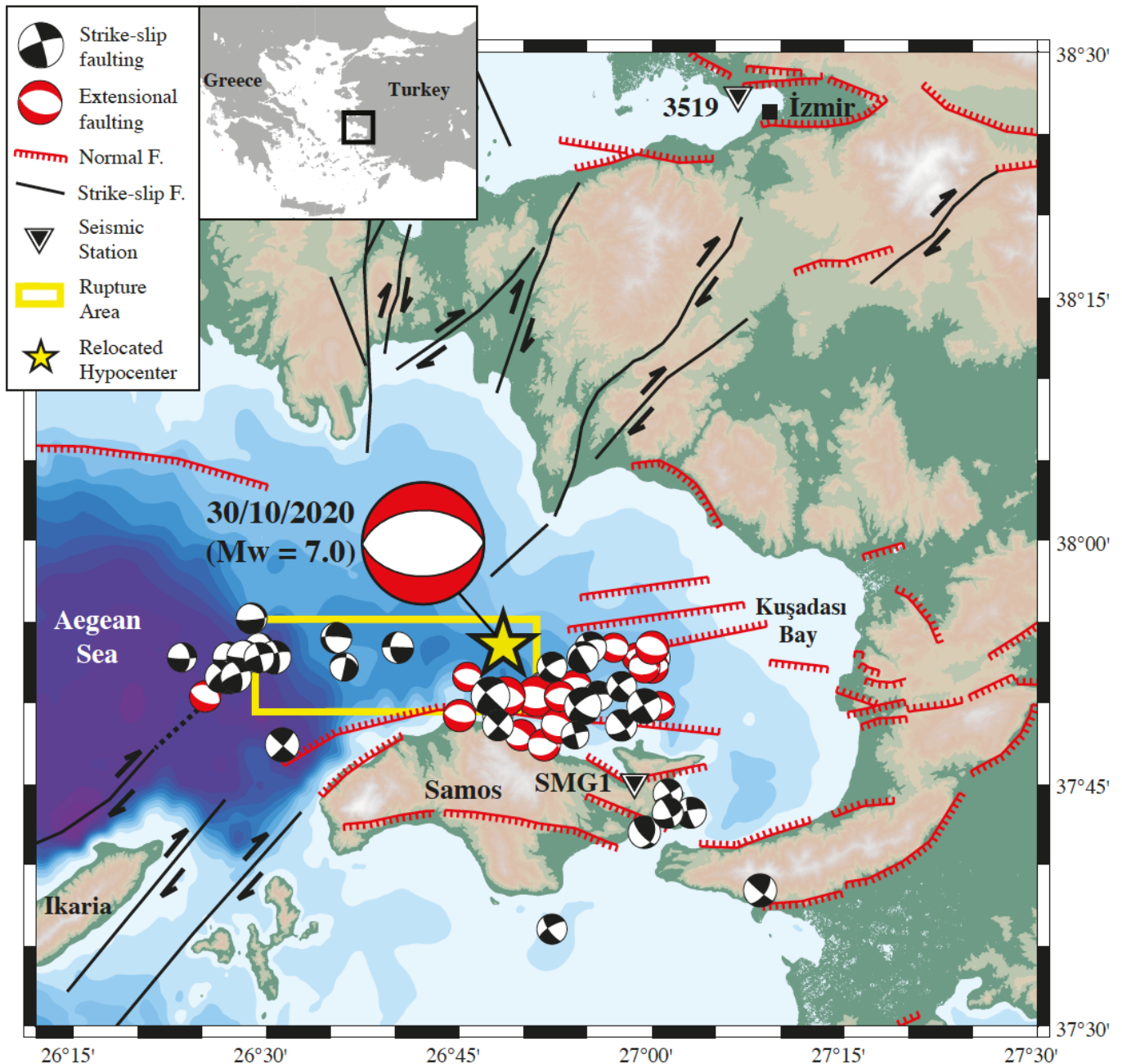

Figure 1. Topography and bathymetry map showing relocated hypocenter (star), rupture area (yellow outlined rectangle) and focal mechanism solution of the 30 October 2020 Samos Earthquake identified from regional waveform modeling (Kiratzi et al., 2020) along with regional moment tensor solutions of aftershocks (Altunel and Pınar, 2020) and active fault segments (compiled from the Neotectonic map of Greece by Mountrakis et al., 2006; Pavlides et al., 2009; Basillic et al., 2013; Uzel et al., 2013; Gürçay 2014; Emre et al., 2018;). Two strong-motion stations near Samos (SMG1) and İzmir (3519) which are used during simulations are also plotted in the map.

2. Coulomb static stress changes

Coulomb static stress changes (ΔCSS) associated with an identified earthquake rupture are useful to evaluate stress loading at nearby faults and commonly correlates spatially well with the aftershocks (King et al., 1994). In this study, the ΔCSS during the Samos earthquake is calculated with the Coulomb 3.3 software (Toda et al., 2011) by assuming an elastic half-space with uniform isotropic elastic properties. Since seismic triggering at nearby faults is considered, slip heterogeneity which can result in large variations within the rupture, is beyond our scope, and thus a homogeneous slip model derived by Kiratzi et al., (2020) is utilized. According to this model, the North dipping W-E trending fault segment with a length of 32 km and width of 15 km is ruptured during the Samos earthquake (Mw 7.0) with an average slip of 2.5 m and a normal mechanism (strike = 270°, dip = 45°, rake = –89°). The rupture initiated at the hypocenter (8.2 km depth) close to rupture bottom depth (11.2 km) and expanded up to ~0.5 km depth beneath sea bottom. This simplified source model is compatible with geodetic (InSAR and GNSS) and seismic (teleseismic, regional and strong motion) data (Ganas et al., 2020, 2021; Sakkas, 2021; Akinci et al. 2021; Karakostas et al., 2021). Poisson's ratio and shear modulus are taken as 0.25 and 3.3×10^5 bar for the earth's crust. In the absence of data related to pore fluid pressure, we adopt 0.4 for the apparent friction. In a transtensional tectonic setting like this one, maximum stress direction may vary significantly, especially in terms of plunge amount. In this respect, plausible regional stress tensors are tested, revealing only minimal variations in amplitude used during simulations. Therefore, the regional stress tensor is not defined, and thus ΔCSS shown in Figure 2 is calculated for receiver faults with kinematics similar to the mainshock.

At 8 km depth, resultant ΔCSS indicates stress loading towards West and East and stress release towards North and South. Relocated aftershocks taken from Kiratzi et al. (2020) correspond spatially well with the positive ΔCSS where stress loading occurs. In this respect, strike-slip fault west of the Ikaria Island merges with aftershocks with strike-slip nature (Figure 1), and faults located within Kuşadası Bay and SE side of the Samos Island are subjected to static stress loading. Aftershock cluster that formed almost instantly in the western tip with dominantly strike-slip mechanisms is located where stress increase reaches up to 10 bars (Figure 2). On the other hand, the delayed aftershock cluster that emerged two days after the mainshock on the SE side of the Island display stress loading is only around 1 bar (Figure 2). Note that the identified positive ΔCSS at these two aftershock clusters will be adopted later in the numerical simulations as static triggering signals.

3. Aftershock evolution in time and space

The spatial and temporal distribution of the relocated aftershocks is shown in Figures 3. The minimal seismic activity observed between longitudes 26.5E and 26.8E matches well with the largest slip identified by finite fault models (Kiratzi et al., 2020; Akinci et al., 2021; Karakostas et al., 2021) and implies efficient stress release in this part of the rupture. The cluster in the western tip (Western cluster) emerges almost instantly, with the largest aftershock (Mw 4.1) appearing ~2 h after the mainshock (star in Figure 3). In contrast, a cluster centered at the SE side of the Island (SE cluster) first emerges ~50 h after the mainshock and reactivated again at ~80 h (Figure 3). This pattern suggests a delayed triggering, such that the Samos earthquake does not
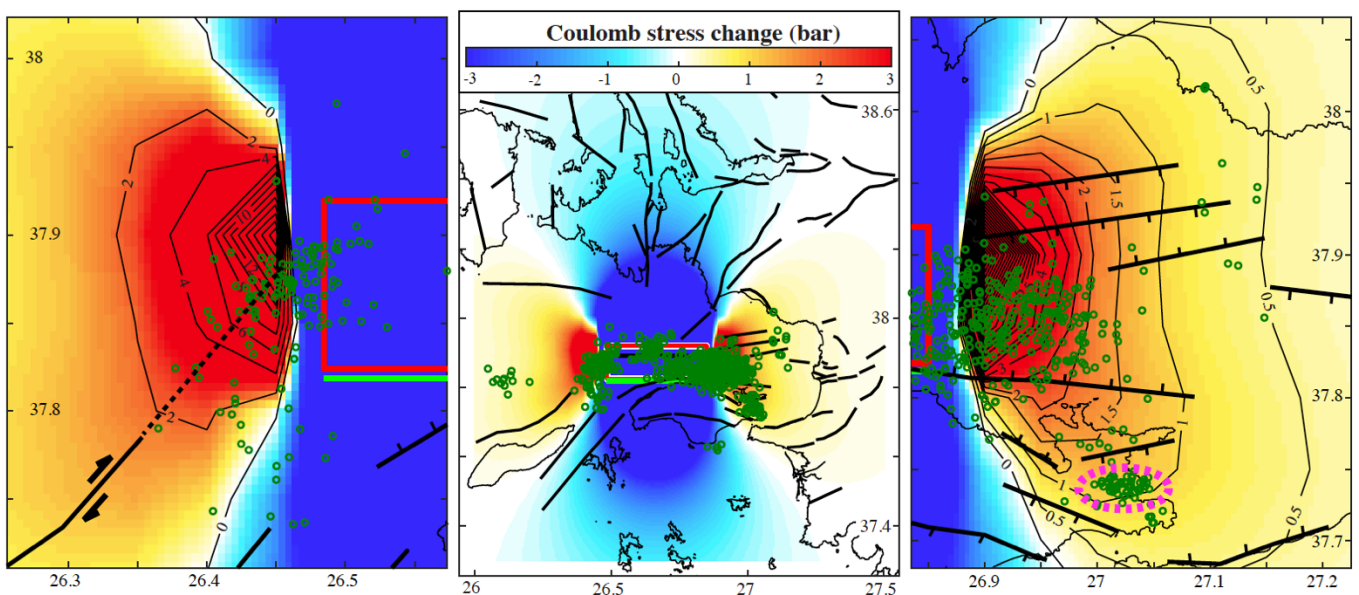

Figure 2. Coulomb static stress changes at a depth of 8 km. The large-scaled map is in the middle, and rupture edge close-ups with contour lines are given on the sides. The red rectangle and green line represent the projected rupture plane and fault trace at the surface, respectively. Solid lines represent faults. The relocated aftershocks shown by green circles are from Kiratzi et al., (2020) which are available online at http://www.geerassociation.org/administrator/components/com_geer_reports/geerfiles/TableS1.cat (accessed on 9.7.2021). The dashed magenta ellipse outlines the location of the SE cluster displaying delayed triggering.
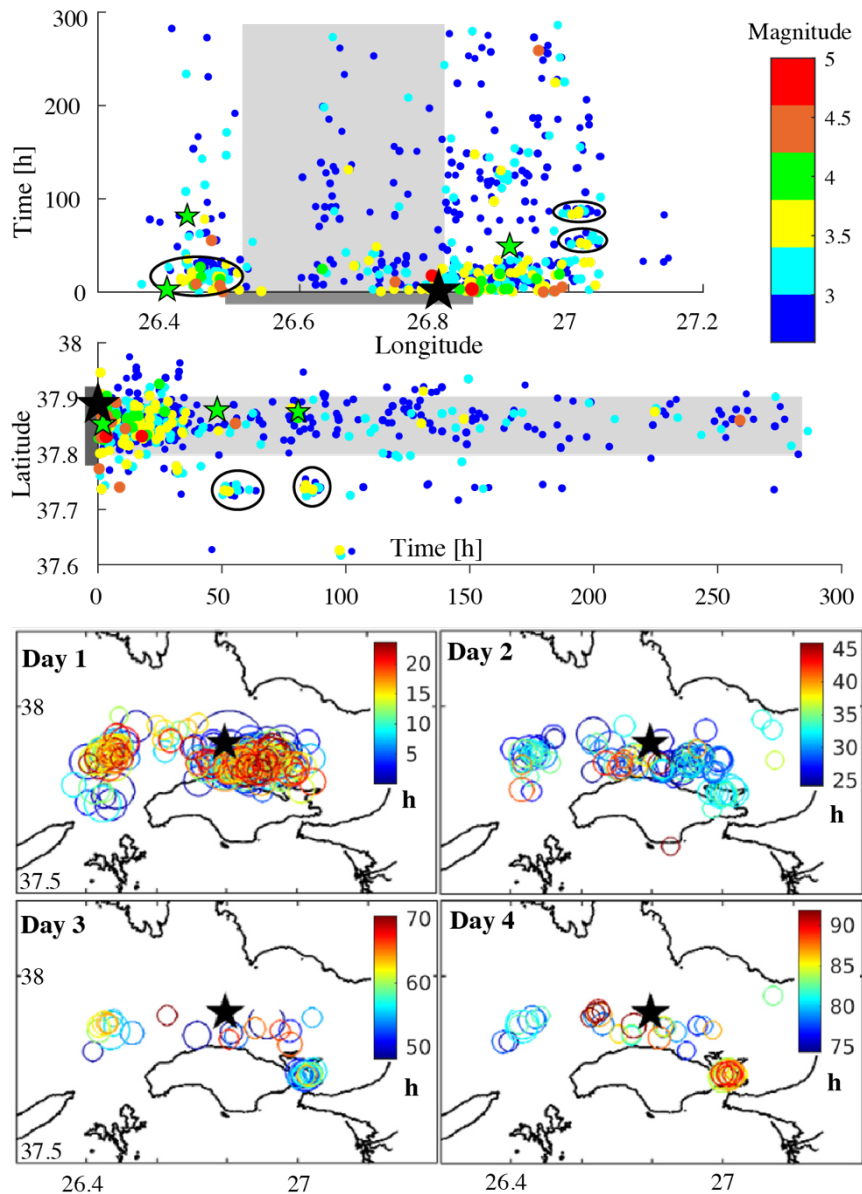
Figure 3. Time versus longitude and latitude plots (at the top) and daily maps (bottom) of relocated aftershocks taken from Kiratzi et al. (2020) (available online, web address is given in the caption of Figure 2). The grey area and ellipses outline the rupture area and aftershock clusters showing almost instant and delayed triggering. The black stars represent the mainshock and large aftershocks (green) within the western cluster and preceding SE cluster at t~50 and 80 h. Note that aftershock data is color-coded according to magnitude (top) and hour of the day (bottom).

instantly lead to fault failure but advances their failure time significantly and thus resulted in time-lapse.

In order to assess the effect of large aftershocks besides the mainshock on the observed delayed triggering, larger magnitude events preceding the SE cluster are examined and plotted (green stars in Figure 3). At t~50 h, the preceding largest event (Mw 4.1) occurred at the eastern edge of the rupture, further North of the SE cluster. The maximum static stress loading associated with this rather low magnitude aftershock that occurs 20 km away from the SE cluster is calculated using an analytical approximation from Chen et al., (2013), given by,

$$\Delta CSS = M_o/(6\pi r^3), \tag{1}$$

where M_o and r denote scalar seismic moment and radius of the asperity patch. According to equation 1, the static stress

load is around only 12 Pa. Thus, its role in triggering is neglected. At t~80 h, the preceding large aftershock (Mw 3.9) is located at the western edge more than 50 km away from the SE cluster and suggests no direct relation with delayed triggering. Besides, even the cumulative effects of aftershocks would not significantly change the SE cluster's stress load.

Furthermore, observations suggest an amplitude-frequency threshold for dynamic triggering to be effective (Brodsky and Prejean, 2005). Our previous study shows that velocity amplitudes higher than 20–30 cm/s and lower frequency content dominance increase the triggering potential for large earthquakes (Sopaci and Özacar, 2020). In this respect, we reasonably assumed that the mainshock's static and dynamic impact instantly triggered the Western cluster and caused delayed triggering at the SE cluster.

4. Numerical simulation

4.1. Methodology and data

We simulate strike and normal type faults using SDF spring slider systems with RSF dependent quasi-dynamic approximation (Rice, 1993). The fault analogies for the vertical and inclined type faults are given in Figure 4.

Of course, the SDF models in Figure 4 are oversimplified approximations and cannot manifest many complex properties of faults. However, as Perfettini et al. (2003b) inferred, SDF results do not differ significantly from a 2D continuum formulation in earthquake triggering works. Besides, complex knowledge beneath the seismogenic region, such as frictional heterogeneity and asperity barrier interaction, etc., are highly unknown. Therefore, we reasonably adopt SDF models to simulate observed triggering events after the Samos rupture. The quasi-dynamic approximation of the equation of motion is given in Equation 2.

$$K\left(\delta_p + X_T(t) - \delta(t)\right) + \Delta\tau(t) + \eta\dot{\delta}(t) = \tau(t) \qquad (2)$$

τ, K, δ_p, δ, η denote frictional stress, fault stiffness, driving plate's slip, block's slip, radiation damping, respectively. We insert permanent static ($\Delta\tau(t)$) and dynamic ($X_T(t)$) perturbation to the system at a specific time. The fault stiffness parameter is approximated with K = G/L, where G and L denote shear modulus and asperity patch length. The radiation damping is approximated by $\eta = G/V_S$ formula, where V_S denotes maximum shear velocity that the slipping block can reach. The RSF law for frictional stress is given in Equation 3.

$$\mu(t) = \tau(t)/\sigma(t) = \mu_0 + a\ln(v(t)/v_p) + \Theta(t) \qquad (3)$$

where μ, μ_0, σ, a, v, v_p denote friction, friction constant, effective normal stress, RSF constitutive parameter for direct velocity effect, block's slip rate ($\dot{\delta}(t) = v(t)$), and the driving plate's slip rate ($\delta_p = v_p$) accordingly. The state variable Θ defines the state of contact history between the frictional surfaces. In this study, we apply the Ruina type state evolution law in Equation 4 (Ruina, 1983) because it provides better performance for dynamic transient effects (Nakatani, 2000; Sopaci and Özacar, 2020).

$$\dot{\Theta}(t) = \frac{-v(t)}{d_C}[\Theta(t) + b\ln(\frac{v(t)}{v_p})] - \alpha\frac{\dot{\sigma}_n(t)}{\sigma_n(t)} \qquad (4)$$

In Equation 4, b denotes the RSF constitutive parameter for the state evolution effect, and d_c is the critical slip distance for renewing a contact between frictional surfaces. We also apply a shear-normal stress coupling relation proposed by Linker and Dieterich (1992) for normal type faults scaled with
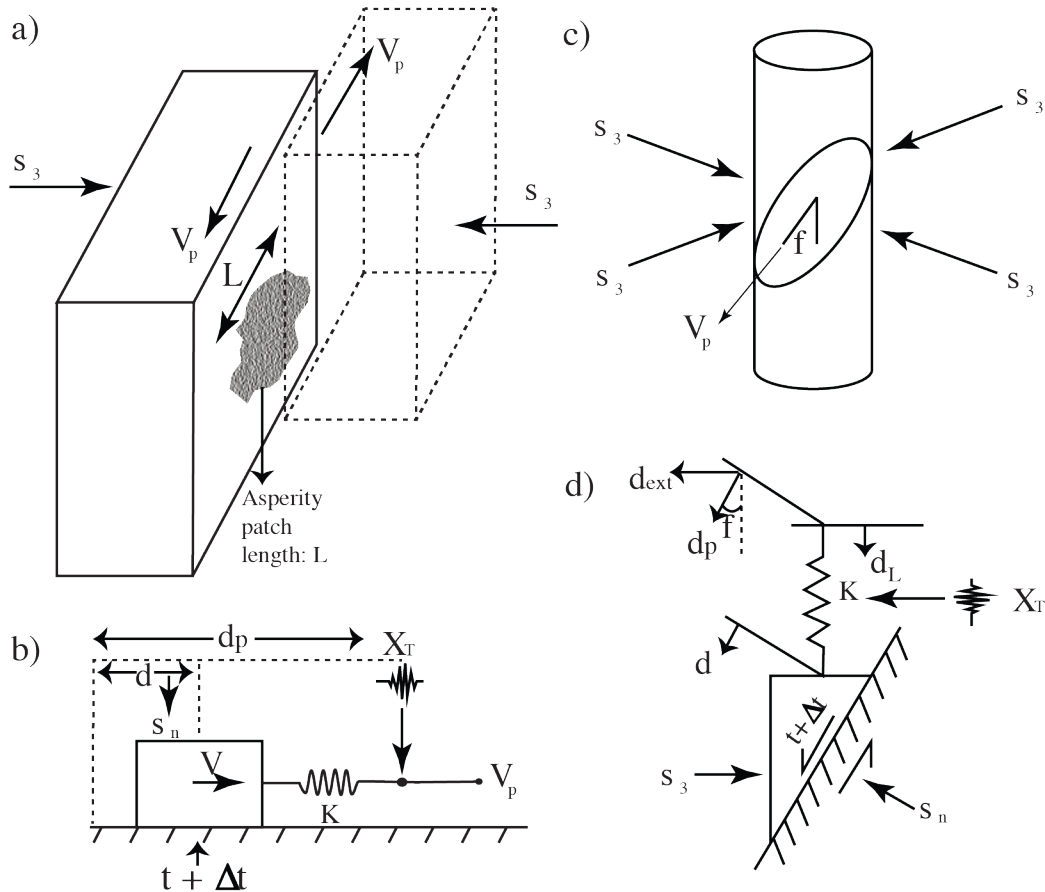

Figure 4. The fault analogies using single-degree-of-freedom (SDF) models. a) vertical strike-slip fault with a single asperity patch, b) spring-slider representation of vertical strike-slip faulting, c) a normal fault with an inclination angle (ϕ), d) spring-slider representation of inclined normal faulting. The figures are redrawn from Gomberg et al. (1997) and Beeler and Lockner (2003) for vertical and inclined faults, accordingly.

a constant α. When shear-normal stress coupling is applied, effective normal stress is computed with Equation 5.

$$\sigma_n(t) = \sigma_3 + \tau \tan \phi \qquad (5)$$

where σ_3 is the minimum principal stress, and ϕ is the inclination angle as sketched in Figure 4. For vertical faults, $\sigma_3 = \sigma_n$, since $\phi = 0$. The parameters utilized during simulations are listed in Table.

The main parameters that control fault's stiffness and earthquake magnitude are asperity patch length and RSF parameters (a and b) (Sopaci, 2019). In this study, the RSF parameters are kept identical to the Gomberg et al. (1997), Belardinelli et al. (2003), and rock friction laboratory works. Instead, we varied the asperity patch length to test the triggering effect on different magnitude earthquakes. For events with Mw < 5, patch length (L) is calculated using the empirical relation between scalar seismic moment (M_o) and circular rupture area (A) from (Wang, 2018), given by

$$M_o A^{3/2} \qquad (6)$$

For earthquakes with Mw < 3.5, ~ 3.5 and 4, L which is equal to the diameter of circular patch is assigned as ~ 0.5, 0.64 and 1.25 km, respectively (Table). On the other hand, large crustal earthquakes are limited in rupture width and may display a high level of slip heterogeneity, and thus, L of characteristic large events are not empirical scaled with seismic moment (M_o) but kept fixed to 5 km following previous simulations works (Wang, 2018; Sopaci and Özacar, 2020). By considering the present ambiguity associated with triggered fault, the range of slip rates (1–5 mm/year) are tested on both vertical strike-slip and 60° dipping normal faults.

During simulations, static and dynamic triggering signals are applied simultaneously to represent the nearby fault segments' combined effect. A modified Coulomb's stress change for static triggering on RSF based model is used (ΔCSS = Δτ – (μ₀ - α) Δσₙ) where Δτ and Δσₙ represent shear and normal stress changes obtained from the Coulomb's solution

near the aftershock clusters (Dieterich et al., 2000; Perfettini et al., 2003b; Yoshida et al., 2020). In this formulation, α, which defines the shear stress change's sensitivity to the normal stress, is taken as 0.5 following Linker and Dieterich (1992). On the other hand, we use real seismic waveforms for dynamic triggering signals. For this purpose, strong motion data recorded by the closest seismic station (SMG1) at Samos Island is used as the dynamic triggering signal.

Furthermore, the potential of a far-field dynamic triggering at faults near the İzmir metropolitan area is simulated using the strong motion record of seismic station (3519) near İzmir Bay which displays the largest recorded ground motions. The selected acceleration records are integrated numerically after trend and mean correction, and then low pass filtered with a cut-off frequency of 20 Hz to eliminate noise in velocity waveform. The resultant velocity waveforms used as dynamic triggers in the simulations and their unfiltered amplitude spectrums displaying attenuated high frequencies at distant recording (3519) near İzmir in comparison to the one (SMG1) near Samos are presented in Figure 5.

5. Simulation results

At first, scenarios analogous to the observed delayed triggering SE side of the Samos Island are established. Centroid solutions of aftershocks within the SE cluster display mixed mechanisms, including normal and strike-slip faulting (Figure 1). Therefore, simulations are constructed for both faulting types using a vertical fault analogy for strike-slip and inclined fault analogy with a dip amount of 60° for normal faulting (Figure 4). During simulations, we applied the shear-normal stress coupling relation of Linker and Dieterich (1992), in which normal stress evolves with shear stress at inclined normal faults and is fixed for vertical strike-slip faults. At the SE cluster where noticeable static stress loading is identified (Figure 2), ΔCSS is defined according to the modified Coulomb's solution as ~1 bar using observed shear and normal stress changes of 0.8 and 1.4 bars, respectively. To evaluate the effect of fault slip rate, which is not well known in this case, we have also tested slip rates of 1, 3, and 5 mm/year.

For each scenario, an undisturbed seismic cycle is established with their recurrence intervals through numerical simulation. Then both static and dynamic triggers are applied simultaneously at different times before failure. The simulation results revealed induced clock advances (simply the difference between the unperturbed and perturbed failure time). The measured clock advances are plotted concerning the triggering signals' onset time in Figure 6a. Since the slip velocity, fault type, and asperity patch length change the stressing rate and, therefore, the recurrence time, the absolute times are normalized by converting the observed clock advance and triggering signals' onset time into percentages with respect to the recurrence time. Owing to the normalization, we visualize results of multiple scenarios comparably (Figure 6b).

According to the simulation results, earthquake triggering is a highly time-dependent process. The dynamic effects
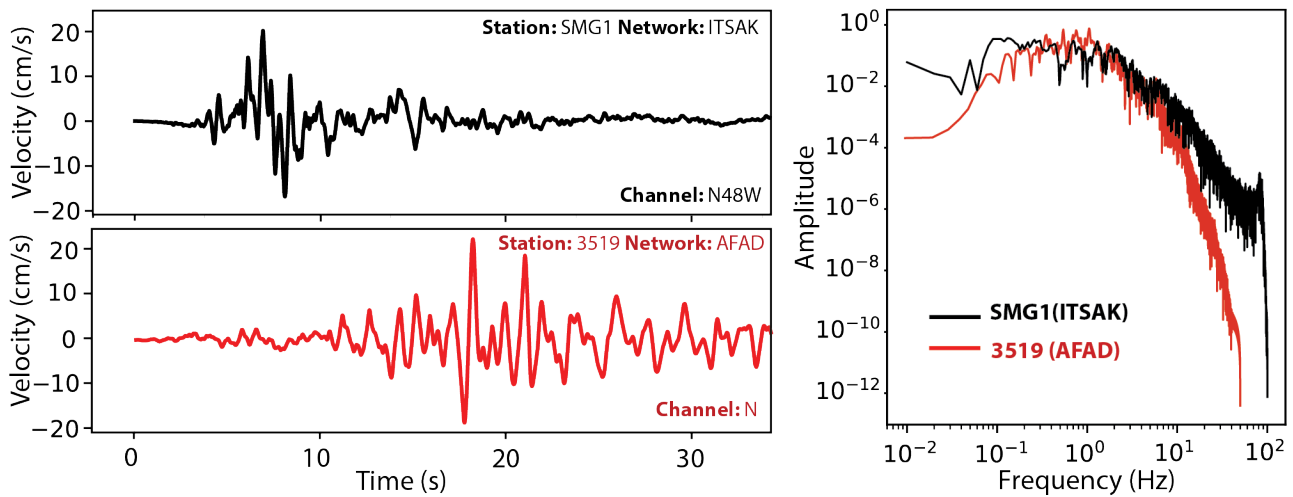
Table. Parameters used in the simulations.

Parameters	Definition	Value
a	Direct velocity effect	0.005
b	State evolution effect	0.01
dc	Critical slip distance	1 mm
α	Shear-normal stress coupling constant	0.5
σ₃	Principle stress	60 MPa
μ₀	Friction coefficient	0.4
G	Shear modulus	33 GPa
Vs	Shear velocity	3.5 km/s
vP	Slip rate on fault plane	1, 3, 5 mm/year
L	Asperity patch length	Characteristic: 5 km Mw~4: 1.25 km Mw~3.5: 0.64 km Mw<3.5: 0.50 km
β	Dip angle (π/2-ϕ)	Strike-slip fault: 90° Normal fault: 60°
ΔCSS	Coulomb static stress change	SE cluster: 1 bar W cluster: 1, 3, 5, 7, 10 bar

Figure 5. The seismic waveforms (on the left) are used for dynamic earthquake triggering and their unfiltered amplitude spectrums (on the right). Station SMG1, located in Samos Island, is operated by the Institute of Engineering Seismology & Earthquake Engineering (ITSAK), and station 3519, located in Karşıyaka, İzmir, Turkey is operated by the Disaster and Emergency Management Presidency of Turkey (AFAD). Check Figure 1 for station locations.

become pronounced when a fault is close to fail and result in a remarkable peak in clock advance (Figure 6). If the time to failure is more than 20% of the earthquake recurrence time (if a fault is not close to failing), the clock advance becomes linear. Hence, it displays only static effects comparable to the stress loading associated with ΔCSS (Figure 6). For the SE cluster, simultaneously simulated static and dynamic triggers do not produce instant seismic triggering at any onset time but rather lead to delayed triggering comparable to the observations when failure time is close.

Moreover, minimal variations identified in normalized clock advance imply that the seismic triggering is not much sensitive to fault slip rate and asperity patch lengths analogous to earthquakes with Mw ≥ 4 (Figure 6b). On the other hand, normal faults display higher normalized clock advance due to static triggering effects suggesting that normal faults are more prone to static stress loading for strike-slip faults. Interestingly, as the dynamic triggering becomes pronounced, simulation results become independent from fault type, and similar values are observed for both strike-slip and normal fault types (Figure 6b).

In absolute time frame, higher clock advances are identified for normal faults characterized by longer recurrence times (Figure 6a). For example, when ~10% of the seismic cycle remains for normal fault failure, clock advance can exceed seven years for triggering a large characteristic earthquake with a recurrence time of over 500 years, which may apply to the faults located SE side of the Samos Island.

Next, scenarios are constructed for vertical strike-slip faulting triggered almost instantly west of the rupture (Figure 1). Considering the observed minimal sensitivity, we fixed the fault slip rate to 3 mm/year. However, a wide range of ΔCSS from 1 to 10 bar is tested to represent stress loading right next to the rupture and slightly further away in agreement with the Coulomb solution (Figure 2). The normalized results are presented together for variable asperity patch lengths and ΔCSS values in Figure 7.

According to our results, small earthquakes with Mw < 3.5 instantly trigger regardless of their position in the seismic cycle, while events with Mw ~ 3.5 instantly trigger depending on the given ΔCSS and triggering signal's onset time. Specifically, instant triggering occurred at ΔCSS of 1, 3, 5, 7, and 10 bars when 10%, 15%, 20%, 27%, and 35% of the seismic cycle is left to fault failure, respectively (Figure 7). The triggering potential of characteristic large earthquakes is also tested by increasing the asperity patch length to 5 km. Results reveal a significant increase in clock advance but do not lead to instant triggering except for very high ΔCSS values (~10 bar).

Finally, the far-field dynamic triggering effect of the Samos earthquake is evaluated on the normal faults located near the İzmir metropolitan area. For this purpose, seismic data of station 3519 located at the İzmir Bay (Figure 1), which displays the largest ground motions recorded in the region (Figure 5), is chosen as the dynamic triggering signal. Although the maximum peak ground velocity of 3519 is comparable to the SMG1 Samos Island station, the simulation analogous to normal faults near İzmir revealed no significant triggering effect on earthquakes' seismic cycle with Mw ≥ 4 (Figure 8).

6. Discussion and conclusion

The seismic triggering potential of an earthquake on nearby or far away faults is hard to quantify due to the present high-level uncertainty associated with friction, fault zone parameters, and onset time of a triggering signal within the seismic cycle. Thus, triggering phenomena have been studied commonly employing laboratory experiments (Beeler and Lockner, 2003; Savage and Marone, 2007, 2008) and numerical simulations (Gomberg et al., 1997, 1998; Belardinelli et al., 2003; Yoshida et al., 2020). It becomes even more challenging at close distances with the nesting of static and dynamic triggering effects (Kilb et al., 2000; Yoshida, 2018). After the 30 October 2020 Samos Earthquake, two
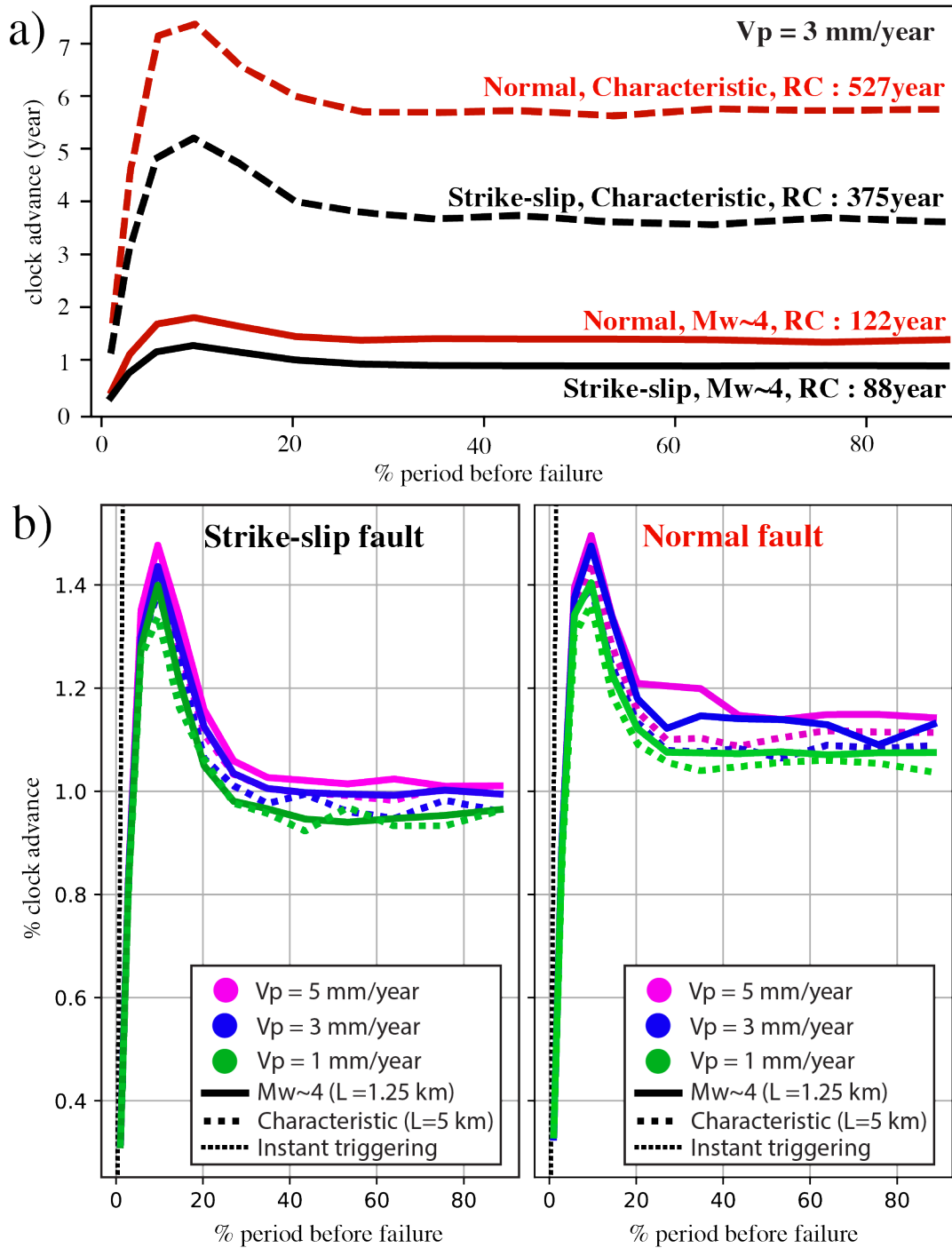
Figure 6. Triggering simulation results of large characteristic and Mw~4 earthquakes with different recurrence times (RC) on normal and strike-slip faults analogous to the delayed triggering observed SE side of the Samos Island. a) absolute clock advance plots for fixed fault slip rate (Vp) of 3 mm/year. b) normalized clock advance plots for variable Vp.

distinct off-plane clusters with maximum Mw~4 are identified, which provided a unique opportunity to study the triggering mechanism of recorded small and moderate-sized earthquakes.

Western cluster associated with strike-slip faulting at the rupture edge is triggered almost instantly. In contrast, the SE cluster has emerged two days after the mainshock further away from the rupture area. The resultant ΔCSS distribution correlates well with the relocated aftershocks. It indicates significant stress loading on the rupture edges that reach 10

bars around the Western cluster and is close to 1 bar across the SE cluster (Figure 2). During simulations, computed ΔCSS values and recorded seismic velocity waveforms are applied simultaneously as static and dynamic triggers for an SDF fault model governed by the RSF law of Ruina (1983).

According to the sensitivity analysis among available RSF laws (Sopaci and Özacar 2020), the chosen Ruina law performs better dynamically but note that usage of alternative views of friction may alter the simulation results. For a particular target fault segment where fault parameters' depth
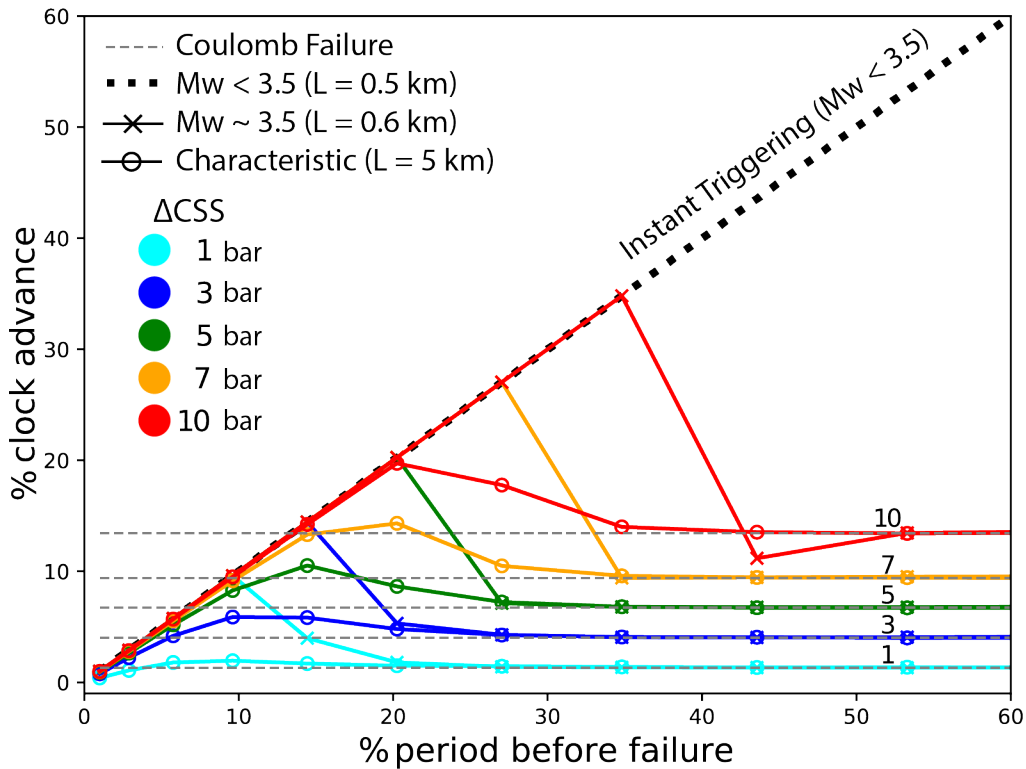
Figure 7. Triggering simulation results of large characteristic, Mw~3.5 and Mw < 3.5 earthquakes on a vertical strike-slip fault for variable Coulomb static stress change analogous to the almost instant triggering observed west of the rupture.
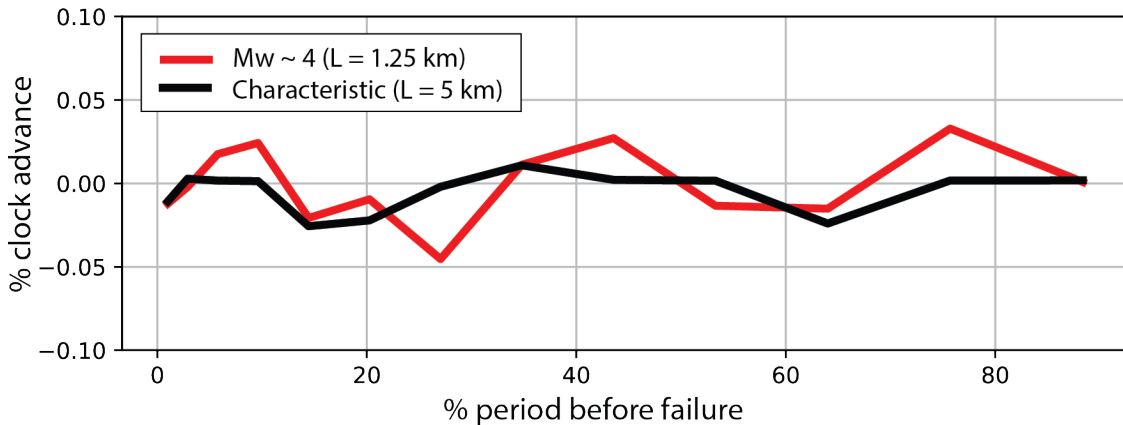

Figure 8. Far-field dynamic triggering simulation results showing normalized clock advance plots of large characteristic and Mw~4 earthquakes on normal faults analogous to faults nearby İzmir.

and lateral variations are well known, more complex 2D-3D continuum formulations can be viable (e.g., Dublanchet et al., 2013; Thomas et al., 2017). However, for laterally uniform fault models, SDF and 2D simulations produce rather similar results (Perfettini et al., 2003b). Due to the lack of data associated with target faults and limited magnitudes of triggered events, complex fault models are kept beyond this study's scope. Nevertheless, our simulations can reasonably mimic the triggered events observed after the Samos Earthquake.

The uniform slip model adopted for the rupture excludes complex static stress changes that may occur within the rupture due to slip heterogeneity and thus not suitable for triggering assessment of aftershocks located within the rupture plane. It is also worth noting that the assumption of

rupture with constant slip may result in artificially higher ΔCSS at close distances to the rupture edge. Similarly, the surface ground motion recorded at nearby seismic stations may exceed the actual motion on the locked deep section of the target faults due to the amplification of seismic waves at the surface. Therefore, dynamic effects may be slightly exaggerated. In this respect, the resultant failure time advances should be treated with caution as the likely maximums.

In general, our results suggest a nonlinear relation to the triggering onset time, compatible with the previous studies (Gomberg et al., 1997, 1998). Dynamic triggering becomes effective only when a fault is closer to fail and significantly increases the clock advance. Otherwise, static triggering effects lead to a rather constant clock advance due to stress

loading comparable with ΔCSS. Our simulations also reveal a sharp decrease in clock advance when failure time is very close, limiting instant triggering (Figure 6). This nonlinear response is associated with the RSF based model, which is different from Coulomb failure models utilizing a constant stress threshold (Gomberg et al., 1998). In this respect, the rare occurrence of instantly triggered moderate or large earthquakes in nature may support its existence.

For small earthquakes (Mw ≤ 3.5), dynamic triggering is more effective and controls the triggering process. The dynamic signals recorded by the seismic station at Samos Island instantly trigger the events with Mw < 3.5 regardless of the onset time. For earthquakes with Mw ~3.5, static effects become more noticeable, and instant triggering is favored by increasing ΔCSS and/or decreasing time to failure (Figure 7). In contrast, the triggering scenarios for Mw ≥ 4 earthquakes result in a significant clock advance but almost always produce delayed triggering events analogous to the SE cluster (Figure 6). However, if ΔCSS takes high values (~10 bar), instant triggering events may occur at the rupture edges like the Western cluster (Figure 7).

Not surprisingly, small earthquakes (Mw ≤ 3.5) are more prone to seismic triggering. Scenarios tested for asperity patch lengths 1.25 and 5 km analogous to Mw~4 and large characteristic earthquakes, respectively, result in surprisingly similar triggering responses (Figure 6). This finding may suggest that earthquakes with Mw ≥ 4 display self-similarity during seismic triggering for a wide range of magnitude. Moreover, the fault slip rate, which defines the recurrence time interval of earthquakes in the target fault, produces a minimal change in normalized clock advances. In other words, the slip rate's uncertainty is not much critical for seismic triggering simulations.

In order to evaluate the effect of target fault type on seismic triggering, both normal and strike-slip analogies are tested. Both fault types reveal very similar responses when a fault is close to failing but differ when stress build-up on the fault is limited (Figure 6). Based on our results, normal faults with inclined fault geometry are more prone to static triggering and display noticeably higher normalized clock advance than strike-slip faults. The applied normal-shear coupling as a function of the dip angle (Beeler and Lockner, 2003) causes such an effect. A change in slip velocity across a dipping fault plane varies normal stress along with shear stress while normal stress remains constant at vertical faults. Unlike here, strike-slip faults can be exposed to normal stress change due to clamping effects that depend on the source and receiver fault positions (Ziv and Rubin, 2000) which cannot be included in our SDF model. Moreover, local fluctuations caused by dynamic transient waves may change fluid pore pressure (Brodsky et al., 2000) and affect normal stress beyond our scope.

According to our results, simulations indicate that the dynamic effects are less pronounced than static effects for earthquakes with Mw ≥ 4. In general, dynamic triggering requires higher amplitude signals to have an equal clock advance with the static triggering (Gomberg et al., 1997; Belardinelli et al., 2003; Yoshida, 2018). According to Sopacı and Özacar (2020), the signals that exceed peak velocity of 30 cm/s produce remarkably more pronounced dynamic impact. At the SMG1 station displaying the largest ground motions recorded nearby, the maximum seismic velocities are around 20 cm/s, limiting the observed dynamic triggering responses in the simulations. Moreover, the dominance of dynamic triggering is highly dependent on the direct velocity effect parameter "a" (Sopaci and Özacar, 2020), which is kept constant according to the previous simulation and laboratory works (Gomberg et al., 1997; Belardinelli et al., 2003). Therefore, lower values of the "a" parameter may significantly increase the dynamic triggering effects (Mancini et al., 2020), or vice-versa (Nagata et al., 2012)

After a damaging earthquake, public living where damaging earthquakes are expected commonly asks whether this event can trigger a large earthquake at faults near to them. The Samos earthquake caused heavy damage concentrated in the İzmir metropolitan area and a high level of public anxiety. Across the Bornova plain, ground motions were amplified anomalously by the thick basin bounded by normal faults from both North and South (Uzel et al., 2013). Static stress changes associated with the Samos earthquake are negligible across İzmir, which is ~70 km away but observed dynamic effects can alter the frictional state of faults with large earthquake potential. In order to provide insight on the far-field dynamic triggering potential of the Samos earthquake, the seismic velocity waveform recorded near İzmir is applied as a dynamic trigger for earthquakes with Mw ≥ 4 on a normal fault. Simulations indicate no significant frictional state change due to dynamic triggering, leading to clock advance (Figure 8).

In conclusion, both instant and delay triggering of earthquakes with Mw ≤ 4 were observed after the Samos earthquake are successfully simulated. Faults adjacent to the rupture are more likely to trigger, particularly the NE-SW trending strike-slip fault bounding the Ikaria Island from the West, producing a large earthquake. In contrast, faults near İzmir remain unaffected by the dynamic triggering of the Samos Earthquake.

References

Akinci A, Cheloni D, Dindar, AA (2021). The 30 October 2020, M7.0 Samos Island (Eastern Aegean Sea) Earthquake: effects of source rupture, path and local-site conditions on the observed and simulated ground motions. Bull. Earthquake Eng. 19: 4745–4771. doi: 10.1007/s10518-021-01146-5

Altunel E, Pınar A (2020). Tectonic implications of the Mw 6.8, 30 October 2020 earthquake in the frame of active faults of Western Turkey. Turkish Journal of Earth Sciences 30: 436-448. doi: 10.3906/yer-2011-6

Basili R, Kastelic V, Demircioglu MB, Garcia Moreno D, Nemser ES et al. (2013). The European Database of Seismogenic Faults (EDSF) compiled in the framework of the Project SHARE, (Share - The European Database of Seismogenic Faults). Project http://diss.rm.ingv.it/share-edsf/. doi: 10.6092/INGV.IT-SHARE-EDSF

Beeler NM, Lockner DA (2003). Why earthquakes correlate weakly with the solid Earth tides: Effects of periodic stress on the rate and probability of earthquake occurrence. Journal of Geophysical Research: Solid Earth 108 (B8) 2391. doi: 10.1029/2001JB001518

Belardinelli ME, Bizzarri A, Cocco M (2003). Earthquake triggering by static and dynamic stress changes. Journal of Geophysical Research: Solid Earth 108 (B3): 1–16. doi: 10.1029/2002JB001779

Brodsky EE, Karakostas V, Kanamori H (2000). A new observation of dynamically triggered regional seismicity: earthquakes in Greece following the August 1999 Izmit, Turkey earthquake. Geophysical Research Letters 27 (17): 1944–8007. doi: 10.1029/2000GL011534.

Brodsky EE, Prejean SG (2005). New constraints on mechanisms of remotely triggered seismicity at Long Valley Caldera. Journal of Geophysical Research: Solid Earth 110: B04302. doi: 10.1029/2004JB003211

Chen KH, Bürgmann R, Nadeau RM (2013). Do earthquakes talk to each other? Triggering and interaction of repeating sequences at Parkfield. Journal of Geophysical Research: Solid Earth 118 (1): 165-182.

Çakir Z, Barka A, Evren E (2003). Coulomb stress interactions and the 1999 Marmara Earthquake sequence. Turkish Journal of Earth Sciences 12: 91-103.

Coban KH, Sayil N (2019). Evaluation of earthquake recurrences with different distribution models in western Anatolia. Journal of Seismology 23 (6): 1405-1422.

Dieterich JH (1979). Modeling of rock friction: 1. Experimental results and constitutive equations. Journal of Geophysical Research: Solid Earth 84 (B5): 2161-2168.

Dieterich J, Cayol V, Okubo P (2000). The use of earthquake rate changes as a stress meter at Kilauea volcano. Nature 408 (6811): 457-460.

Dublanchet P, Bernard P, Favreau P (2013). Interactions and triggering in a 3-D rate-and-state asperity model. Journal of Geophysical Research: Solid Earth 118 (5): 2225-2245.

Emre Ö, Duman TY, Özalp S, Şaroğlu F, Olgun Ş et al. (2018). Active fault database of Turkey. Bulletin of Earthquake Engineering 16: 3229-3275.

Ganas A, Elias P, Briole P, Tsironi V, Valkaniotis S et al. (2020). Fault responsible for Samos earthquake identified. Temblor. doi: 10.32858/temblor.134

Ganas A, Elias P, Briole P, Valkaniotis S, Escartin J et al. (2021). Co-seismic and post-seismic deformation, field observations and fault model of the 30 October 2020 M w = 7.0 Samos earthquake, Aegean Sea. Acta Geophysica 69: 999–1024. doi: 10.1007/s11600-021-00599-1

Gomberg J, Blanpied ML, Beeler NM (1997). Transient triggering of near and distant earthquakes. Bulletin of the Seismological Society of America 87 (2): 294-309.

Gomberg J, Beeler NM, Blanpied ML, Bodin P (1998). Earthquake triggering by transient and static deformations. Journal of Geophysical Research: Solid Earth 103 (B10): 24411-24426.

Gürçay S (2014). Sığacık Körfezi ve çevresinin denizaltı aktif tektoniğinin yüksek çözünürlüklü sismik yöntemler uygulanarak araştırılması. PhD, Dokuz Eylül University, İzmir, Turkey, (in Turkish)

Karakaisis GF (2000). Effects of zonation on the results of the application of the regional time predictable seismicity model in Greece and Japan. Earth, planets and space 52 (4): 221-228.

Karakostas V, Tan O, Kostoglou A, Papadimitriou E, Bonatis P (2021). Seismotectonic implications of the 2020 Samos, Greece, M$_w$ 7.0 mainshock based on high-resolution aftershock relocation and source slip model Acta Geophys 69 997. doi: 10.1007/s11600-021-00637-y

Kilb D, Gomberg J, Bodin P (2000). Triggering of earthquake aftershocks by dynamic stresses. Nature 408 (6812): 570-574.

King GC, Stein RS, Lin J (1994). Static stress changes and the triggering of earthquakes. Bulletin of the Seismological Society of America 84 (3): 935-953.

Kiratzi A, Özacar AA, Papazachos C, Pınar A (2020). Coordinators of Chapter 1: Regional tectonics and seismic source. In: Cetin KO, Mylonakis G, Sextos A, Stewart JP (editors). Seismological and Engineering Effects of the M 7.0 Samos Island (Aegean Sea) Earthquake. GEER-069. doi: 10.18118/G6H088

Linker MF, Dieterich JH (1992). Effects of variable normal stress on rock friction: Observations and constitutive equations. Journal of Geophysical Research: Solid Earth 97(B4): 4923-4940.

Mancini S, Segou M, Werner MJ, Parsons T (2020). The predictive skills of elastic Coulomb rate-and-state aftershock forecasts during the 2019 Ridgecrest, California, earthquake sequence. Bulletin of the Seismological Society of America 110 (4): 1736-1751. doi: 10.1785/0120200028

Mountrakis D, Kilias A, Vavliakis E, Psilovikos A, Karakaisis G et al. (2006). Neotectonic Map of Greece, "Samos" sheet, scale 1:75.000 78 p.

Nagata K, Nakatani M, Yoshida S (2012). A revised rate-and state-dependent friction law obtained by constraining constitutive and evolution laws separately with laboratory data. Journal of Geophysical Research: Solid Earth 117 B02314. doi: 10.1029/2011JB008818

Nakatani M (2000). Conceptual and physical clarification of rate and state friction: Frictional sliding as a thermally activated rheology. Journal of Geophysical Research: Solid Earth 106 (B7): 13347-13380.

Nanjo KZ (2020). Were changes in stress state responsible for the 2019 Ridgecrest, California, earthquakes? Nat Commun 11 3082. doi: 10.1038/s41467-020-16867-5

Pavlides S, Tsapanos T, Zouros N, Sboras S, Koravos G et al. (2009). Using Active Fault Data for Assessing Seismic Hazard: A Case Study from NE Aegean Sea, Greece. In: Earthquake Geotechnical Engineering Satellite Conference XVIIth International Conference on Soil Mechanics & Geotechnical Engineering 2-3/10/2009; Alexandria, Egypt. pp: 1-14

Perfettini H, Schmittbuhl J, Cochard A (2003a). Shear and normal load perturbations on a two-dimensional continuous fault: 1. Static triggering. Journal of Geophysical Research: Solid Earth 108 (B9): 2408. doi: 10.1029/2002JB001804

Perfettini H, Schmittbuhl J, Cochard A (2003b). Shear and normal load perturbations on a two-dimensional continuous fault: 2. Dynamic triggering. Journal of Geophysical Research: Solid Earth 108 (B9): 2409. doi: 10.1029/2002JB001805

Rice JR (1993). Spatio-temporal complexity of slip on a fault. Journal of Geophysical Research: Solid Earth (B6): 9885– 9907. doi:10.1029/93JB00191.

Ruina A (1983). Slip instability and state variable friction laws. Journal of Geophysical Research: Solid Earth 88 (B12): 10359-10370.

Sakkas V (2021). Ground Deformation Modelling of the 2020 Mw6.9 Samos Earthquake (Greece) Based on InSAR and GNSS Data. *Remote Sensing* 13 (9): 1665. doi: 10.3390/rs13091665

Savage HM, Marone C (2007). Effects of shear velocity oscillations on stick-slip behavior in laboratory experiments. Journal of Geophysical Research: Solid Earth 112: B02301. doi: 10.1029/2005JB004238

Savage HM, Marone C (2008). Potential for earthquake triggering from transient deformations. Journal of Geophysical Research: Solid Earth. 113: B05302. doi: 10.1029/2007JB005277.

Sopaci E (2019). Hız-ve-durum sürtünme yasaları ve Burridge-Knopoff yay blok sistemi kullanılarak depremlerin dinamik modellenmesi. Jeodezi ve Jeoinformasyon Dergisi 6 (2): 115-127. (In Turkish with English abstract)

Sopaci E, Özacar AA (2020). Investigation of Dynamic and Static Effects on Earthquake Triggering Using Different Rate and State Friction Laws and Marmara Simulation. EGU General Assembly Online, 4– 8 May 2020, EGU2020-533. doi: 10.5194/egusphere-egu2020-533

Thomas MY, Avouac JP, Lapusta N (2017). Rate-and-state friction properties of the Longitudinal Valley Fault from kinematic and dynamic modeling of seismic and aseismic slip. Journal of Geophysical Research: Solid Earth 122 (4) 3115-3137.

Toda S, Stein RS, Sevilgen V, Lin J (2011). Coulomb 3.3 Graphic-rich deformation and stress-change software for earthquake, tectonic, and volcano research and teaching—user guide. US Geological Survey open-file report 1060: 63.

Uzel B, Sözbilir H, Ozkaymak C, Kaymakçı N, Langeris CG (2013). Structural evidence for strike-slip deformation in the İzmir-Balıkesir Transfer Zone and consequences for late Cenozoic evolution of western Anatolia (Turkey). Journal of Geodynamics 65: 94–116.

van der Elst NJ, Savage HM (2015). Frequency dependence of delayed and instantaneous triggering on laboratory and simulated faults governed by rate-state friction. Journal of Geophysical Research: Solid Earth 120 (5): 3406-3429.

Wang JH (2018). A review on scaling of earthquake faults. Terrestrial, Atmospheric & Oceanic Sciences 29: 589-610. doi: 10.3319/TAO.2018.08.19.01

Yoshida S (2018). Numerical simulations of earthquake triggering by dynamic and static stress changes based on a revised friction law. Journal of Geophysical Research: Solid Earth 123 (5): 4109-4122.

Yoshida S, Maeda T, Kato N (2020). Earthquake triggering model based on normal-stress-dependent Nagata law: application to the 2016 Mie offshore earthquake. Earth, Planets and Space 72 (1): 1-13.

Ziv A, Rubin AM (2000). Static stress transfer and earthquake triggering: No lower threshold in sight? Journal of Geophysical Research: Solid Earth 105 (B6): 13631-13642.